Supplementary Information

Enhanced interlayer neutral excitons and trions in trilayer van der Waals heterostructures

Chanyeol Choi[1,2,9,†], Jiahui Huang[1,2], Hung-Chieh Cheng[3,4], Hyunseok Kim[2], Abhinav Kumar Vinod[1,2], Sang-Hoon Bae[3,4,10], V. Ongun Özçelik[5], Roberto Grassi[6], Jongjae Chae[3], Shu-Wei Huang[1,2,11], Xiangfeng Duan[4,7], Kristen Kaasbjerg[8], Tony Low[6], and Chee Wei Wong[1,2,†]

[1] Fang Lu Mesoscopic Optics and Quantum Electronics Laboratory, University of California, Los Angeles, CA 90095, United States

[2] Department of Electrical Engineering, University of California, Los Angeles, CA 90095, United States

[3] Department of Materials Science and Engineering, University of California, Los Angeles, CA 90095, United States

[4] California Nanosystems Institute, University of California, Los Angeles, CA 90095, United States

[5] Andlinger Center for Energy and the Environment, Princeton University, Princeton, New Jersey 08544, United States

[6] Department of Electrical and Computer Engineering, University of Minnesota, Minneapolis, MN 55455, United States

[7] Department of Chemistry and Biochemistry, University of California, Los Angeles, CA 90095, United States

[8] Center for Nanostructured Graphene (CNG), Department of Micro- and Nanotechnology (DTU Nanotech), Technical University of Denmark, DK-2800 Kgs. Lyngby, Denmark

[9] Present address: Department of Electrical Engineering and Computer Science, Massachusetts Institute of Technology, Cambridge, MA 02139, United States

[10] Present address: Department of Mechanical Engineering, Massachusetts Institute of Technology, Cambridge, MA 02139, United States

[11] Present address: Department of Electrical, Computer, and Energy Engineering, University of Colorado Boulder, Boulder, CO 80309, United States

[†] Corresponding authors: cowellchoi@gmail.com ; cheewei.wong@ucla.edu

Content

S1. Computed band structures of single-layer (SL) $MoSe_2$ and WSe_2
S2. Two interlayer excitons radiative recombination pathways
S3. Integrated photoluminescence (PL) intensity in bilayer and trilayer heterostructures
S4. Full width half maximum (FWHM) of two interlayer excitonic states
S5. Semiconductor bandgap renormalization with temperature
S6. Time-resolved photoluminescence (TRPL) with different excitation wavelengths
S7. Cryogenic micro-PL measurement of individual WSe_2 and $MoSe_2$ monolayer
S8. Cryogenic PL mapping of the trilayer heterostructure
S9. Mass-action model analysis of interlayer exciton trion concentration

S1. Computed band structures of single-layer (SL) MoSe$_2$ and WSe$_2$

Figure 1 shows the results of computed band structures for SL MoSe$_2$ and WSe$_2$, based on the spin-polarized density functional theory (DFT) within the generalized gradient approximation (GGA) using the same set of parameters as presented in the main text. Both of these SL structures have D_{3h} group symmetry without inversion symmetry and have a direct band gap at the K point. The lattice constants of both MoSe$_2$ and WSe$_2$ SL structures are calculated as 3.33 Å with a nearest neighbor Mo(W) – Se distance of 2.54 Å. In the electronic structure calculations, when the spin-orbit coupling is excluded, the spin-up and spin-down valence bands are degenerate at the K point. However, spin-orbit interaction splits these bands from each other by 0.18 eV and 0.47eV at the K point for MoSe$_2$ and WSe$_2$ respectively. On the other hand, the spin-orbit interaction at the conduction band minimum is much lower, 0.02 eV for MoSe$_2$ and 0.03 eV for WSe$_2$. Here it should be noted that at the K point the valence band maximum is dominated by the d_{x2-y2} and d_{xy} orbitals of the Mo/W atoms and the conduction band minimum is dominated by the d_{z2} orbitals of the Mo/W atom. It should also be noted that the chalcogen atom Se has no contribution to the VBM or CBM at the K point.
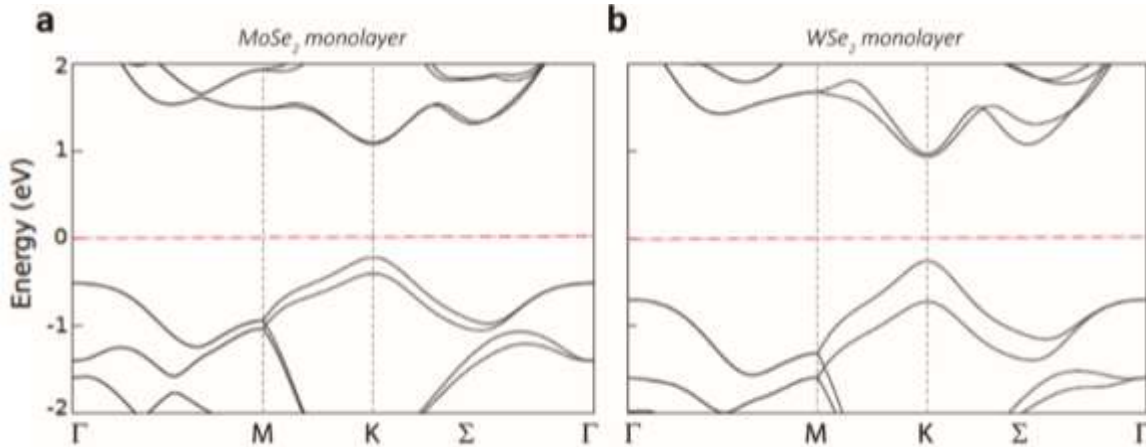
Figure S1 | Computed band structures of single-layer MoSe$_2$ and WSe$_2$. a, Computed band structure of SL MoSe$_2$. **b,** Computed band structure of SL WSe$_2$.
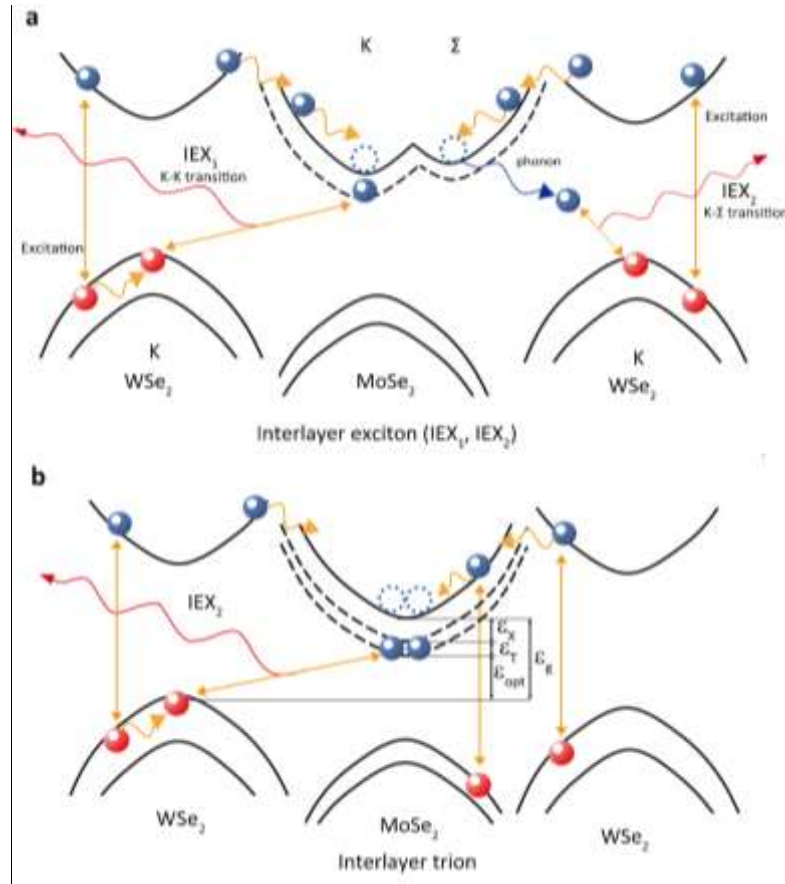
S2. Two interlayer excitons radiative recombination pathways

Figure S2 shows two possible ways to explain a lower energy peak: one is another interlayer exciton (IEX$_2$) and the other is interlayer trion. As for explanation of another interlayer exciton described in Figure S2a, while IEX$_1$ occurs at the same momentum space (K-K transition), IEX$_2$ occurs through pathway placing on different momentum space (K-Σ transition). To make it feasible, the energy variance between the Σ edge at MoSe$_2$ conduction band and K edge at WSe$_2$ valence band should be on the same order-of-magnitude as the energy caused by thermal fluctuation. When it comes to explanation of interlayer trion as illustrated in Figure S2b, trions are generated through interaction between interlayer exciton and electron due to electron accumulation in MoSe$_2$ conduction band minimum on a picosecond timescale [S1,S2]. In effect,

we can obtain the trion binding energy (ε_T) through the power-dependent photoluminescence. The tuning effect of three-body excitonic system results from the strong quantum-confined Stark effect [S3]. The energy splitting between interlayer neutral exciton and trion is expressed [S4]:

$$\omega_I - \omega_X = E_{Trion} + \Delta E \tag{S1}$$

where E_{Trion} is the trion binding energy and ΔE is the energy required for one carrier to be promoted into the free-carrier system. $\omega_I - \omega_X$ denotes the minimum energy for the removal of one electron from the trion, because the exciton is regarded as an ionized trion [S5]. ΔE becomes negligible when the Fermi surface increases with high carrier injection since the initial doping level (E_F) is less significant as a result of the enhanced carrier screening effect by carrier injection in 2D systems [S6]. In our case, we can expect high quantum PL yield, efficient charge transfer, and large effective mass of the carriers in the trilayer heterostructures. Therefore, ΔE becomes negligible and $\omega_I - \omega_X$ can be taken as the trion binding energy [S4]. In our trilayer heterostructure, trion binding energy is ≈ 27 meV, which deduced from Figure 4b.


Figure S2 | Illustration of two pathways for interlayer exciton radiative recombination, and the interlayer trions model. a, Illustration of two different interlayer excitons radiative recombination pathways: one is K-K direct transition in *k*-space and the other is K-Σ indirect transition in *k*-space. In the case of indirect transitions, phonon is involved to match the momentum difference, which lowers the energy bandgap. **b,** Schematic summary of the

interlayer trion radiative recombination predicted by a type-II heterojunction in our trilayer vdWs heterostructure. ε_X, ε_T, ε_{opt} and ε_g represent exciton binding energy, trion binding energy, optical bandgap and electronic bandgap, respectively. This is an example in the formation of the interlayer trions: two electrons in $MoSe_2$ and one hole in WSe_2.

S3. Integrated photoluminescence (PL) intensity in bilayer and trilayer heterostructures

To compare bilayer heterostructure with trilayer heterostructure, integrated PL intensities are measured at ≈ 0.2 mW and with an ≈ 1 μm laser spot size. As shown below, ≈ 3 times brighter PL intensity (and ≈ 30 meV lower energy PL peak) of trilayer heterostructure is observed at 77 K. To show the PL intensity difference of two different heterostructures, we collected the below data in the same bath temperature and excitation time duration by one dimensional InGaAs focal plane array detector. The noise here is caused by the absence of filters, only for this measurement.
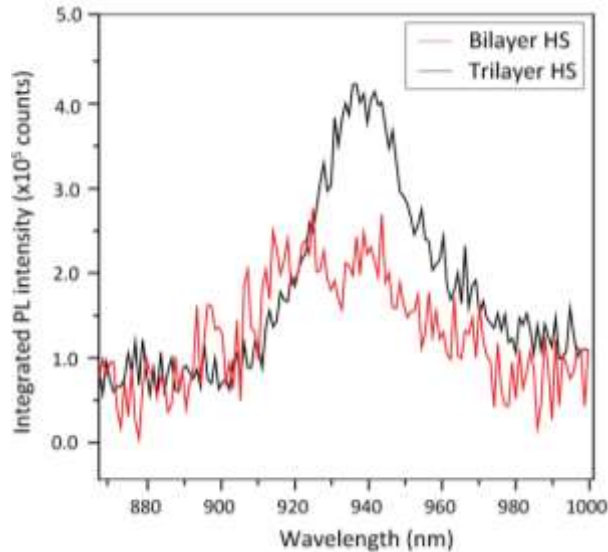

Figure S3 | Integrated PL intensities in bilayer and trilayer heterostructures. This comparison demonstrates the brighter PL emission in WSe_2-$MoSe_2$-WSe_2 trilayer heterostructure than WSe_2-$MoSe_2$ bilayer heterostructure, enabled by the tightly overlapping wavefunctions and additional absorbance from the extra WSe_2 layer in the trilayer heterostructure.

S4. Full-width half-maximum (FWHM) of two interlayer excitonic states

Figure S4 plots the FWHM of the two interlayer excitonic states. In order to see the temperature effects on the interlayer excitonic states, we extrapolated both sets of FWHM data from Figure 3b and note that IEX_2 features a much broader FWHM than IEX_1. From 4 K to 96 K, we can see that the FWHM of two interlayer excitonic states is almost constant with increasing temperature, with the interlayer trion (IEX_2) showing a larger width. The tendency of not broadening with increasing temperature suggests that there are more processes, such as defect

scattering or other radiative recombination, contributing to the FWHM other than electron-phonon interactions [S7].
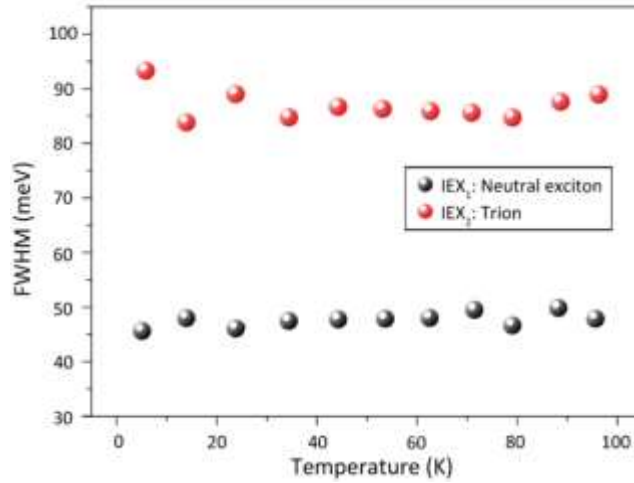
Figure S4 | Full-width half-maximum (FWHM) of two interlayer excitonic states. FWHM of interlayer exciton and trion in the trilayer heterostructure as a function of the bath temperatures.

S5. Semiconductor bandgap renormalization with temperature

In Figure 3c the two PL peaks of excitonic states (neutral exciton and trion) are fitted by temperature-bandgap renormalization model as below [S8]:

$$E_g(T) = E_g(0) - S\langle\hbar\omega\rangle\left[\coth\left(\frac{\langle\hbar\omega\rangle}{2K_bT}\right) - 1\right] \tag{S2}$$

where $E_g(0)$ represents the band gap at zero temperature, S is a dimensionless coupling constant, and $\langle\hbar\omega\rangle$ is an average phonon energy. The above describes the phonon-induced gap reduction with temperature and we fit the neutral exciton peak shift (solid lines in Figure 3c) with corresponding $E_g(0) \approx 1.331$ eV (interlayer neutral exciton ground-state transition energy, 0 K), $S \approx 0.006$ and $\langle\hbar\omega\rangle \approx 6.0$ meV. The trion peak is also fitted by values for $S \approx 0.012$, $\langle\hbar\omega\rangle \approx 9.9$ meV, and $E_g(0) \approx 1.284$ eV (interlayer trion ground-state transition energy, 0 K). The energy splitting between the two excitonic states peaks is ≈ 47 meV at 4 K, with 1.96 eV pump and 1.2 mW pump power. It decreases with lower pump power and is ≈ 27 meV at 0.01 mW pump. We focus on the measured data from 4 K to 245 K since above 245 K the PL signals from interlayer neutral exciton and trion become almost indistinguishable from the noise.

S6. Time-resolved photoluminescence (TRPL) with different excitation wavelengths

In addition to the temperature-dependent lifetime measurements, we also performed TRPL measurements by varying the excitation wavelengths to explore the electron-phonon decay dynamics of the interlayer neutral exciton in the trilayer heterostructure. As shown in Figure S6a,

the wavelengths of excitation pulse pump range from 510 nm (green) to 660 nm (red). In each measurement, we selected bandpass filters to exclude the effect of pump side-peaks before our trilayer sample. We further performed TRPL measurements for the interlayer trion; however, its comparably lower photon counts and weaker pump excitation pulse energy below 600 nm does not allow a lifetime to be meaningfully obtained. We also note that our tunable pulse laser has different pulsewidths for different pump excitation wavelengths as shown in Figure S6b. The extracted carrier lifetimes, with a summary shown in Figure S6c, are on the order of nanoseconds and significantly longer than the picosecond pump pulsewidth variations.
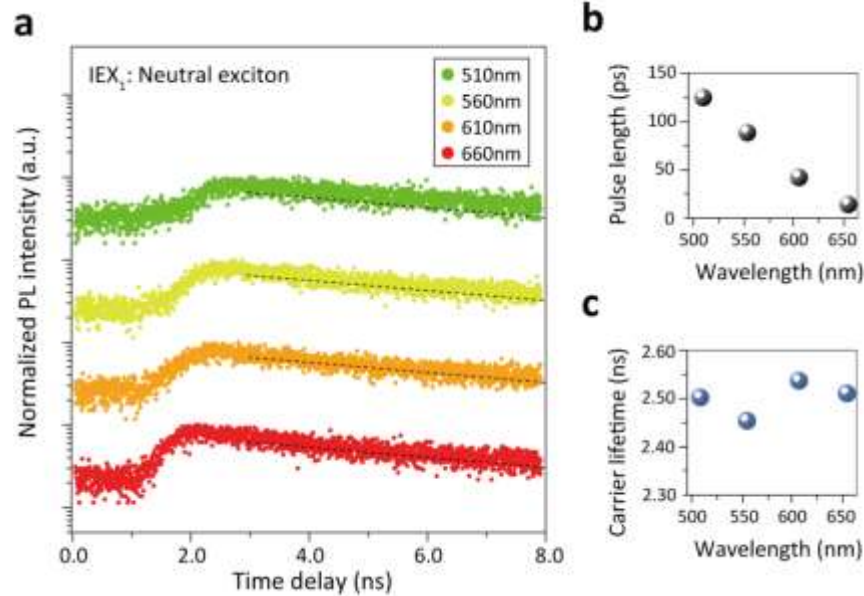
Figure S6 | Carrier lifetimes for various excitation wavelengths. a, Interlayer exciton lifetime as a function of excitation wavelengths at 4 K. Photoluminescence intensities are normalized and fitted with biexponential decay functions. **b,** Excitation pulsewidths as function of excitation wavelengths, from the pump laser. **c,** Measured carrier lifetimes deduced from panel **a**.

### S7. Cryogenic micro-PL measurement of individual WSe_2 and $MoSe_2$ monolayers

Defect trapped localized exciton recombination may generate localized PL emission at low temperature. Previous studies observed PL emission of localized excitons of monolayer $MoSe_2$ and WSe_2 at 1.58 to 1.66 eV and 1.64 to 1.69 eV [S9-S11]. However, the existence of localized emission around 1.28 and 1.33 eV is unknown. To rule out the possibility that the interlayer emission are from the localized exciton, we performed cryogenic micro-PL measurement of the $MoSe_2$ and WSe_2 monolayers from the same bulk crystal, examining from 1.18 to 1.58 eV as shown in Figure S7. No localized emission is observed in the 1.28 and 1.33 eV region.
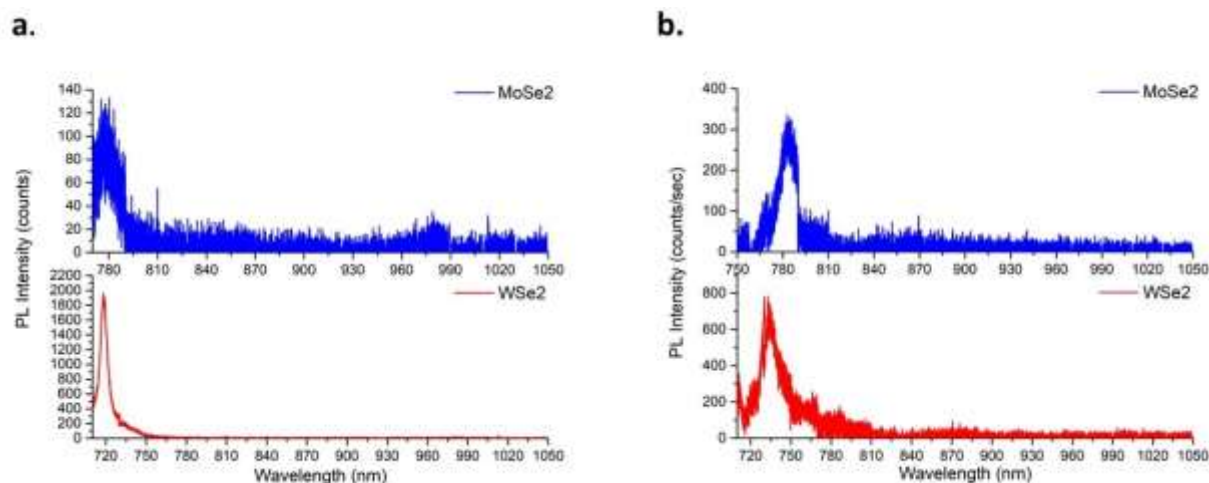
Figure S7 | Cryogenic micro-PL measurement of individual monolayer MoSe$_2$ and WSe$_2$ from the same bulk. a, micro-PL measurement of monolayer MoSe$_2$ and WSe$_2$ from the same bulk at 77 K. **b,** micro-PL measurement of monolayer MoSe$_2$ and Wse$_2$ from the same bulk at 4 K. Both measurements are using the 660 nm laser excitation.

S8. Cryogenic PL mapping of trilayer heterostructure

Previous studies of the strain effect on the stacked van der Waals heterostructures and 2D materials have reported the PL spectral shift and intensity change due to tensile strain and strain-induced effects, like the strain-induced indirect-to-direct bandgap transition [S12, S13]. To clarify the strain effect in the trilayer heterostructure, the PL intensity mapping around the trilayer region at 77 K is performed Only interlayer PL is collected by using the 850 nm long pass filter. As shown in figure S8, the trilayer heterostructures is possessing a uniform PL intensity over the interlayer spectral window. The transition region (yellow region in figure S8) between high and low intensity is due to the program averaging when the laser spot is on the edge of the trilayer flake and slightly out-of-focus of the laser. This can confirm with the expectation that less strain effects, such as bending a substrate during the material transfer processes, are involved or the strain is uniform on the sample so that the strain is not a major impact in our study.
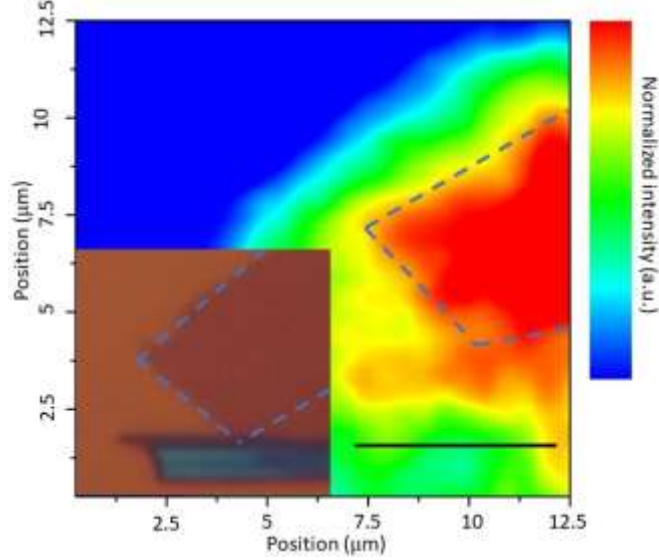
Figure S8 | Cryogenic PL intensity mapping of trilayer heterostructure with 850 nm long pass filter. The trilayer region is excited by 660 nm with 200 µW power (on sample) at 77 K. Blue dash line: trilayer sample region. Scale bar: ~5 µm.

S9. Mass-action model analysis of interlayer exciton trion concentration

From Figure S4, the linewidth of interlayer exciton and trion PL are almost constant with temperature change. So the integrated PL of the two peaks using Lorentz fitting is proportional to the peak PL intensity. We can therefore relate the PL peak intensity ratio (Figure 3e) to the ratio of concentrations of trions to excitons and use the mass action model to observe:

$$\frac{n_{X-}}{n_X} \sim \frac{n_e \exp(\frac{E_T}{k_B T})}{k_B T} \tag{S3}$$

where n_{X-}, n_X and n_e are the concentration of natural excitons, trions and free electrons. E_T is the trion binding energy. The variations of the three variables with temperature and the doping level are reported by Ross *et al* [S14]. $n_B = n_{X-} + n_e$ is the doping level and should be a constant. At non-zero doping levels then n_{X-} and n_e will show a sharp increase at low temperature and n_X will be small. The $\frac{n_{X-}}{n_X}$ ratio would therefore show a sudden increase at low temperature as shown in Figure 3e. The abrupt rise around 10 K is a key feature of trions as mentioned in the main text. And that also agrees with the abrupt change in n_{X-} and n_X as predicted by Ross *et al* [S14]. Notice that the abrupt change only occurs when there is sufficient doping level so that there is large formation of trions.

Supplementary References

S1. Lin, Y., Ling, X., Yu, L., Huang, S., Hsu, A. L., Lee, Y. H., Kong, J., Dresselhaus, M. S., Palacios, T. Dielectric screening of excitons and trions in single-layer MoS2. *Nano Letters* 2014; **14**: 5569–5576.

S2. Efimkin, D. K., Macdonald, A. H. Many-body theory of trion absorption features in two dimensional semiconductors. *Physical Review B* 2017; **95**: 035417.

S3. Miller, D. A. B., Chemla, D. S., Damen, T. C., Gossard, A. C., Wiegmann, W., Wood, T. H., Burrus, C.A. Band-edge electroabsorption in quantum well structures: The quantum-confined stark effect. *Physical Review Letters* 1984; **53**: 2173–2176.

S4. Jones, A. M., Yu, H., Ghimire, N. J., Wu, S., Aivazian, G., Ross, J. S., Zhao, B., Yan, J., Mandrus, D. G., Xiao, D., Yao, W., Xu, W. Optical generation of excitonic valley coherence in monolayer WSe_2. *Nature Nanotechnology* 2013; **8**: 634–638.

S5. Mak, K. F., He, K., Lee, C., Lee, G. H., Hone, J., Heinz, T. F., Shan, J. Tightly bound trions in monolayer MoS_2. *Nature Materials* 2013; **12**: 207–211.

S6. Yang, J., Xu, R., Pei, J., Myint, Y. W., Wang, F., Wang, Z., Zhang, S., Yu, Z., Lu, Y. Optical tuning of exciton and trion emissions in monolayer phosphorene. *Light: Science and Applications* 2015; **4**: e312.

S7. Molina-Sánchez, A., Palummo, M., Marini, A., Wirtz, L. Temperature-dependent excitonic effects in the optical properties of single-layer MoS_2. *Physical Review B* 2016; **93**: 155435.

S8. O'Donnell, K. P., Chen, X. Temperature dependence of semiconductor band gaps. *Applied Physics Letters* 1991; **58**: 2924–2926.

S9. Chakeaborty, C., Goodfellow, K. M., Vamivakas, A. N., Localized emission from defects in MoSe2 layers. *Optical Materials Express* 2016; **6**: 2081-2087.

S10. Wang, G., Bourt, L., Lagarde, D., Vidal, M., Balocchi, A., Amand, T., Marie, X., Urbaszek, B. Valley dynamics probed through charged and neutral exciton emission in monolayer WSe2. *Physical Review B* 2014; **90**: 075413.

S11. Godde, T., Schmidt, D., Schmutzler, J., Aßmann, M., Debus, J., Withers, F., Alexeev, E. M., Pozo-Zamudio, O. D., Skrypka, O. V., Novoselov, K. S., Bayer, M., Tartakovskii A.I. Exciton and trion dynamics in atomically thin MoSe2 and WSe2: Effect of localization. *Physical Review B* 2016; **94**: 165301.

S12. He, Y., Yang, Y., Zhang, Z., Gong, Y., Zhou, Wu., Hu, Z., Ye, G., Zhang, X., Bianco, S., Jin, Z., Zou, X., Yang, Y., Zhang, Y., Xie, E., Lou, J., Yakobson, B., Vajtai, R., Li, B., Ajayan, P. Strain-induced electronic structure changes in stacked van der Waals heterostructures. *Nano Letters* 2016; **16**: 3314-3320.

S13. Ahn, G. H., Amani, M., Rasool, H., Lien, D.-H., Mastandrea, J. P., Ager III, J. W., Dubey, M., Chrzan, D. C., Minor, A. M., Javey, A. Strain-engineered growth of two-dimensional materials. *Nature Communications* 2017; **8**: 608.

S14. Ross, J. S., Wu, S. F., Yu, H. Ghimire., N. J., Jones, A. M., Aivazian, G., Yan, J., Mandrus, D. G., Xiao, D., Yao, W., Xu, X. Electrical control of neutral and charged excitons in a monolayer semiconductor. *Nature Communications* 2013; **4**: 1474.